Shape factor for dual-permeability fractured reservoir simulation
Effect of non-uniform flow in 2D fracture network

Gong, J.; Rossen, W. R.

DOI
10.1016/j.fuel.2016.06.113

Publication date
2016

Document Version
Final published version

Published in
Fuel: the science and technology of fuel and energy

Fuel 184 (2016) 81–88

Contents lists available at ScienceDirect

Fuel

journal homepage: www.elsevier.com/locate/fuel

Full Length Article

Shape factor for dual-permeability fractured reservoir simulation: Effect of non-uniform flow in 2D fracture network

J. Gong *, W.R. Rossen

Department of Geoscience & Engineering, Delft University of Technology, Delft 2628 CN, The Netherlands

ARTICLE INFO

Article history:
Received 25 June 2015
Received in revised form 14 April 2016
Accepted 23 June 2016
Available online 8 July 2016

Keywords:
Shape factor
Dual-permeability
Dual-porosity
Fractured reservoir

ABSTRACT

The flow properties of naturally fractured reservoirs are dominated by flow through the fractures. In a previous study we showed that even a well-connected fracture network behaves like a much sparser network when the aperture distribution is broad enough: i.e., most fractures can be eliminated while leaving a sub-network with virtually the same permeability as the original fracture network. In this study, we focus on the influence of eliminating unimportant fractures which carry little flow on the inferred characteristic matrix-block size. We model a two-dimensional fractured reservoir in which the fractures are well-connected. The fractures obey a power-law length distribution, as observed in natural fracture networks. For the aperture distribution, because information from the subsurface is limited, we test a number of cases: log-normal distributions (from narrow to broad), and power-law distributions (from narrow to broad). The matrix blocks in fractured reservoirs are of varying sizes and shapes; we adopt the characteristic radius and the characteristic length to represent the characteristic matrix-block size. We show how the characteristic matrix-block sizes increase from the original fracture network to the dominant sub-network. This suggests that the matrix-block size, or shape factor, used in dual-porosity/dual-permeability waterflood or enhanced oil recovery (EOR) simulations or in homogenization should be based not on the entire fracture population but on the sub-network that carries almost all of the injected fluid (water or EOR agent).

1. Introduction

Naturally fractured reservoirs contain a significant amount of hydrocarbon reserves worldwide [1], However, the oil recovery from these reservoirs has been rather low. The low level of oil recovery indicates that more accurate reservoir characterisation and flow simulation is needed.

Reservoir simulation is one of the most practical methods of studying flow problems in porous media. For fractured reservoir simulation, the dual-porosity/dual-permeability concept and the discrete fracture model are two typical methods [2]. In the dual-porosity/dual-permeability approach, the fracture and matrix systems are treated as separate domains; interconnected fractures serve as fluid flow paths between injection and production wells, while the matrix acts only as fluid storage, and these two domains are connected with an exchange term [3–5]. In a dual-permeability model, fluid flow can also take place between matrix grid blocks, unlike from the dual-porosity model [6,7]. In order to simulate the realistic fracture geometry and account explicitly for the effect of individual fractures on fluid flow, discrete-fracture models have been developed [8–14]. Compared to the dual-porosity/dual-permeability models, discrete-fracture models represent a fracture network more explicitly and make the simulation more realistic. But discrete fracture models are typically difficult to solve numerically. Thus, although dual-porosity/dual-permeability models are much simplified characterizations of naturally fractured reservoirs, they are still the most widely used methods for field-scale fractured-reservoir simulation, as they address the dual-porosity nature of fractured reservoirs and are computationally cheaper. To generate a dual-porosity/dual-permeability model, it is necessary to define average properties for each grid cell, such as porosity, permeability and matrix-fracture interaction parameters (typical fracture spacing or shape factor) [15]. Therefore, the discrete fracture network considered to generate the dual-porosity model parameters is crucial. Using homogenization, one can treat matrix-fracture exchange more accurately than in dual porosity/dual permeability simulations [16], but, again, one needs a characteristic matrix-block size.

As we presented in a previous study [17], even in a well-connected fracture network, there is a dominant sub-network

* Corresponding author.
E-mail addresses: j.gong@tudelft.nl (J. Gong), w.r.rossen@tudelft.nl (W.R. Rossen).

http://dx.doi.org/10.1016/j.fuel.2016.06.113
0016-2361/

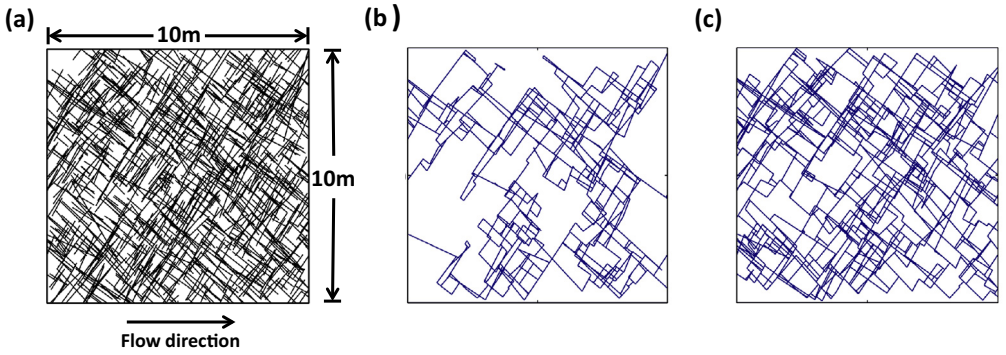

Fig. 1. (a) One realization of the fracture network examined in this study. The size of the fractured region is 10 m × 10 m × 0.01 m. The left and right boundaries are each at fixed hydraulic head; the difference in hydraulic head is 1 m. Water flows from left to right; the top and bottom edges are no-flow boundaries. (b) Dominant sub-network for one realization with a power-law aperture distribution with $\alpha = 1.001$. (c) Dominant sub-network for one realization with a power-law aperture distribution with $\alpha = 2$.

which carries almost all the flow, but it is much more sparse than the original network (Fig. 1). The flow-path length of the dominant sub-network can be as little as roughly 30% of that of the corresponding original fracture network in the most extreme case. This suggests that in secondary production, the water injected flows mainly along a small portion of the fracture network. In contrast, in primary production even relatively small fractures can be an efficient path for oil to flow to a production well.

This paper is organized as follows: we first introduce the numerical model and research process. Next, we analyse the sizes of the matrix blocks formed by the entire fracture network and the corresponding dominant sub-network. Finally, we point out the implications of this distinction for the dual-porosity/dual-permeability reservoir simulation.

2. Models

Since this is a follow-up study to our previous research [17], the models used here are the same as the ones adopted before (Fig. 1). Here we only introduce the models briefly; more details can be found in the previous work. Fracture networks are generated in a 10 m × 10 m × 0.01 m region using the commercial fractured-reservoir simulator FracMan™ [18]. Two fracture sets which are nearly orthogonal to each other are assumed, with almost equal numbers of fractures in the two sets. Each fracture, with a rectangular shape, is located following the Enhanced Baecher Model and is perpendicular to the plane which follows the flow direction and penetrates the top and bottom boundaries of the region. Because of the uncertainties in data and the influence of cut-offs in measurements, fracture-trace lengths have been described by exponential, log-normal or power-law distributions in previous studies [19–21]. Commonly, a power-law distribution is assumed by many researchers to be the correct model for fracture length [22–25], with exponent α ranging from 1.5 to 3.5. In this study, the fracture length follows the power-law distribution ($f(x)$):

$$f(x) = \frac{\alpha - 1}{x_{min}} \left(\frac{x_{min}}{x}\right)^{\alpha} \tag{1}$$

where α is the power-law exponent, x is the fracture length and x_{min} the lower bound on x, which we take to be 0.2 m. In order to make sure that there are no extremely short or long fractures, and in particular that opposite sides of our region of interest cannot be connected by a single fracture, we choose $\alpha = 2$ and truncate the length distribution on the upper end at 6 m. Since even the smallest fracture length (0.2 m) is much larger than the thickness of the region of interest (0.01 m), the 3D model can be seen as a 2D fracture network.

For fracture apertures, two kinds of distribution which have been proposed in previous studies are adopted: power-law [26–31] and log-normal [32–37]. In each kind of distribution, to include the entire range of feasible cases (from narrow to broad aperture distribution), different parameter values (α for a power-law aperture distribution and σ for a log-normal aperture distribution) are examined. The aperture is randomly assigned to each fracture.

The power-law distribution can also be defined as:

$$f(x) = x^{-\alpha} \tag{2}$$

If the power-law aperture distribution is described by Eq. (2), the studies cited above found that the value of the exponent α in nature is 1, 1.1, 1.8, 2.2, or 2.8. In this study, the power-law aperture distribution is defined by Eq. (1) as well as the fracture length distribution, where x stands for aperture instead of length. Eq. (1) differs from Eq. (2), in that it includes a minimum cut-off value, and α should be larger than 1. To include the entire range of feasible cases (from narrow to broad aperture distribution), here we examine α in the range from 1.001 to 6. In each case, the fracture aperture is limited to the interval between 0.01 mm and 10 mm. The aperture range can vary greatly in different formations; it also depends on the resolution and the size of the region studied. According to the field data collected from the Ship Rock volcanic plug in NW New Mexico [38] and Culpeper Quarry and Florence Lake [39], the aperture range [0.01 mm, 10 mm] adopted here is realistic, at least at some locations in natural.

The log-normal distribution is specified by the following probability density function:

$$f(x) = \frac{1}{x \log_{10}(\sigma)\sqrt{2\pi}} \exp\left\{-\frac{1}{2}\left(\frac{\log_{10}(x) - \mu}{\sigma}\right)^2\right\} \tag{3}$$

where μ and σ are the mean and the standard deviation in the log-10 space. The truncated log-normal distribution has two additional parameters: a minimum and a maximum value of aperture. Field studies and hydraulic tests found values of σ from 0.1 to 0.3, 0.23, and 0.47 [32,35,40]. To test the widest range of feasible values, we test values of σ from 0.1 to 0.6. More details can be found in our previous study [17]. In order to focus on the influence of fracture aperture distributions on the dominant sub-network, except for the aperture distribution, all the other parameter distributions remain the same for all the cases tested in this study, including the fracture length, the orientation, etc.

We assume that a fracture can be approximated as the slit between a pair of smooth, parallel plates; thus the aperture of each fracture is uniform. Steady state flow through the fractured region is considered (Fig. 1a). In this paper, we consider that fracture permeability is much greater than matrix permeability, which is

common in fractured reservoirs [41,42]. The flow regimes of fractured formations can be defined by the fracture-matrix permeability ratio. Especially, if the ratio is greater than 10^5–10^6, fractures carry nearly all the flow [43,44]. Since we are interested in the non-uniform flow in well-connected fracture networks for characterizing flow in the fracture network, the matrix is further assumed to be impermeable, so that fluid flow can take place only in the fracture network, similar to the flow regime between fractures and permeable rock mass with the fracture-matrix permeability ratio is greater than 10^5–10^6. Assuming zero matrix permeability is merely a convenient assumption for calculating flow in fracture networks. For computing flow in discrete fracture networks, as in most numerical simulation methods, Darcy's Law for steady-state incompressible flow is employed, and mass is conserved at each intersection of fractures. In our models, we induce fluid flow from the left side to the right side by applying a constant difference in hydraulic head across the domain, while all the other boundaries are impermeable. Mafic™, a companion program of FracMan™, is employed to simulate flow in the fracture networks.

3. Methodology

As presented in the previous study, even in a well-connected fracture network, when the aperture distribution is broad enough, there is a dominant sub-network which can be a good approximation of the actual fracture network. This dominant sub-network is also strongly affected by the aperture distribution. The "dominant sub-network" is defined as the sub-network obtained by eliminating a portion of fractures while retaining 90% of the original-network equivalent permeability There is no special meaning for this 90% threshold, we choose it to illustrate the effect of non-uniform flow. In this study, our main interest lies in examining the change of the characteristic sizes of matrix blocks as more fractures are eliminated. We also check the influence of aperture distribution (exponent α in a power-law distribution and standard deviation σ in a log-normal distribution) on the characteristic sizes of matrix blocks formed by the dominant sub-network. A Matlab program is employed to calculate the characteristic matrix block sizes. The equivalent matrix block size is employed to represent the average value of the resulting distribution of matrix block sizes.

The approach used to decide which portion of fractures to remove is as follows. Mafic™ subdivides the fractures into finite elements for the flow calculations. The flow velocity at the centre of each finite element and the value of flow velocity × aperture ($=Q_{nodal}$) can be obtained. Based on this value, we compute the average value (Q) of all the elements in each fracture. Q is then used as the criterion to eliminate fractures: fractures are eliminated in order, starting from the one with the smallest value of Q to the one with the largest Q. That is to say, the fractures that conduct the least flow are eliminated first. After each step, we calculate the equivalent network permeability of the truncated network.

Because the generation of the fracture network is a random process, an infinite number of fracture networks can be generated with the same parameter values for the density, the orientation, the fracture length and the aperture distribution. In this study, for each set of parameter values, we generate one hundred realizations.

4. Characteristic matrix block sizes

The matrix blocks in fractured reservoirs can be of varying shapes and sizes. In order to quantitatively study the size and the recovery behaviour of the matrix blocks, several parameters have been proposed [45–49]. In this study, we adopt the characteristic radius and the characteristic length.

Zimmerman and Bodvarsson [50] argued that an irregularly-shaped matrix block can be modelled with reasonable accuracy as a spherical matrix block. The effective radius of the corresponding spherical block is defined as

$$r = \frac{3V}{S} \tag{4}$$

where V is the volume of the matrix block, and S is the surface area. They also proposed that in the early-time regime (shortly after a change in the boundary condition imposed at the block surfaces), a series of spherical blocks with variable radii can be modelled using uniform blocks with an equivalent radius given by:

$$r_e = \left(\sum_{i=1}^{n} \frac{V_i}{V_t} r_i^{-1} \right)^{-1} \tag{5}$$

where n is the number of matrix blocks, i refers to one matrix block, r_i is the effective radius of that matrix block, V_i is the volume of that matrix block and V_t is the total matrix volume. In this study, we adopt a similar idea to define the characteristic matrix-block radii of 2D fractured formations. The characteristic radius of each irregularly-shaped matrix block is defined as:

$$r_i = \frac{2S_{mi}}{L_{mi}} \tag{6}$$

where i refers to one matrix block, S_{mi} is the area of the matrix block, and L_{mi} is the perimeter of the two-dimensional matrix block.

The equivalent matrix-block radius is then defined as:

$$r_e = \left(\sum_{i=1}^{n} \frac{S_i}{S_t} r_i^{-1} \right)^{-1} \tag{7}$$

where n is the number of matrix blocks, i refers to one matrix block, S_i is the area of that matrix block and S_t is the total matrix area.

The second parameter used in this study for representing the matrix-block size is the characteristic length, which was first proposed by Kazemi et al. [46] and followed by other researchers [47,51,52]. Kazemi et al. [46] proposed a shape factor (F_s) of a single matrix block for the imbibition process, which considered the effect of matrix-block shapes and boundary conditions:

$$F_{si} = \frac{1}{V_{mi}} \sum_{j=1}^{n} \frac{A_j}{d_j} \tag{8}$$

where i refers to one matrix block, V_{mi} is the volume of that matrix block, j refers to one face of that matrix block which is open to imbibition, A_j is the area of that face, d_j is the distance from that face to the centre of the matrix block, and n is the total number of faces of the matrix block open to imbibition. This shape factor is claimed to be valid for anisotropic matrix blocks with irregular shapes [53].

The characteristic length of an irregular matrix block L_c is then defined as

$$L_{ci} = \frac{1}{\sqrt{F_{si}}} \tag{9}$$

In fractured reservoirs, the matrix block is the main location for storage of oil and it feeds the surrounding fractures; thus the bulk volume of the matrix is vital to the recovery rate. Therefore, we believe that a volume-weighted equivalent length is more reasonable than a number-based average value. An equivalent length for a series of matrix blocks is then represented as

$$L_e = \left(\sum_{i=1}^{n} \frac{V_i}{V_t} L_{ci}^{-1} \right)^{-1} \tag{10}$$

where i refers to one matrix block, V_i is the volume of that matrix block, L_{ci} is the characteristic length of that matrix block, and V_t is the total bulk volume of the matrix blocks.

In this study, the equivalent radius (r_e) and the equivalent length (L_e) defined above are used to represent the average size of the matrix blocks in a fractured region. Only fractures that belong to the spanning cluster are included in calculating the matrix block sizes; the dead-ends are systematically removed from the network. Also, the matrix blocks containing impermeable boundaries (i.e. along the top and bottom of the region of interest) are not considered. Only the matrix blocks formed by the fractures which have fluid flow through them and the permeable left and right boundaries are taken into account.

5. Results

In this section, we present the results for the cases with power-law aperture distributions (from narrow to broad) and log-normal aperture distributions (from narrow to broad).

5.1. Results for cases with power-law aperture distribution

Fig. 2 shows the normalized area-weighted harmonic-average of characteristic matrix radii (r_e^b). The scatter in Fig. 2a–c reflects the difference among the 100 realizations; the average trend curves are shown in Fig. 2d. As presented in Fig. 2, as more fractures are eliminated, the length of the backbone of the truncated fracture network (l_b) decreases, while the equivalent radius of the matrix blocks formed by the fracture network (r_e^b) increases. The average trends are very close to each other for the cases with different values of power-law aperture distribution exponent α, no matter whether the apertures distribute broadly or narrowly (Fig. 2d). The normalized equivalent permeability of the truncated fracture network (K_b) is shown in Fig. 3 in which K_b/K_o is the ratio between the equivalent permeability of the dominant sub-network (K_b) and the equivalent permeability of the original fracture network (K_o), while l_b/l_o represents the ratio between the length of the backbone of the truncated fracture network (l_b) and the total length of the original fracture network (l_o). The results show that the dominant sub-network (the sub-network retaining 90% of the original equivalent network permeability after eliminating a portion of fractures) is strongly affected by the aperture distribution: for the broadest aperture distribution cases ($\alpha = 1.001$), the flow-path length (l_b) is roughly 35% of the total length of the original fracture network (l_o), while for the narrowest aperture distribution ($\alpha = 6$), the ratio of l_b/l_o is approximately 0.6 (Fig. 3). Correspondingly, as presented in Fig. 2d, the equivalent matrix radius for the dominant sub-network is on average about twice that for the original fracture network when $\alpha = 1.001$ (the red dashed line), while the ratio is approximately 1.5 for the cases with the narrowest aperture distribution with $\alpha = 6$ (the red dotted line).

Fig. 4 shows the characteristic radii (r_c) of all the individual matrix blocks formed by the entire fracture network and the dominant sub-networks (retaining 90% of original-network equivalent permeability) for one realization for each value of α (Fig. 4). The vertical axis ("CDF") shows for each case the portion of fractures with r_c greater than the given value. In general, the characteristic radii of the matrix blocks formed by the dominant sub-network are larger than those formed by the entire fracture network. The reason is that the dominant sub-network contains fewer of the original fractures [17].

The other parameter used in this paper to represent the sizes of matrix of varying shapes is the characteristic length which is defined in Eqs. (8) and (9). In Fig. 5, we show the normalized equivalent matrix length (L_e^b) of the truncated fracture network, while in Fig. 6, the characteristic length (L_c) distribution of the individual matrix blocks formed by the original fracture network and the

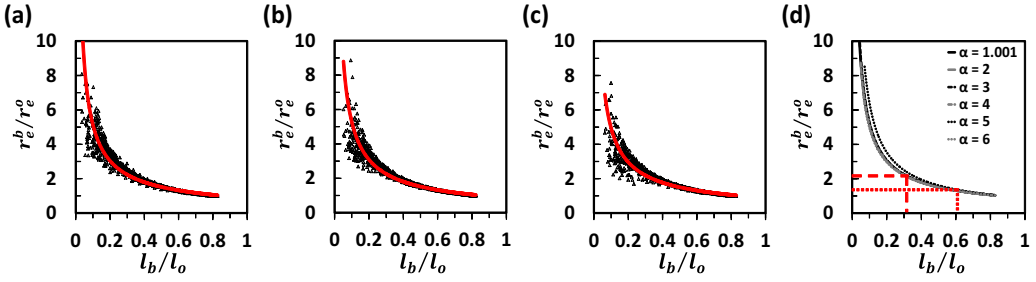

Fig. 2. Equivalent matrix radius of the dominant sub-network (r_e^b) normalized by the equivalent matrix radius of the original fracture network (r_e^o), plotted against the length of the backbone of the truncated fracture network (l_b) normalized by the total length of the original fracture network (l_o): power-law aperture distributions with (a) $\alpha = 1.001$, (b) $\alpha = 2$ and (c) $\alpha = 6$. Results of 100 realizations are shown for each value of α. The red curve is the average trend curve. (d) Average curves from (a–c), including additional values of α. Also shown are values of l_b/l_o for the sub-network retaining 90% of the equivalent network permeability (Fig. 3) and resulting values of r_e^b/r_e^o for $\alpha = 1.001$ (red dashed line) and $\alpha = 6$ (red dotted line), respectively. (For interpretation of the references to color in this figure legend, the reader is referred to the web version of this article.)

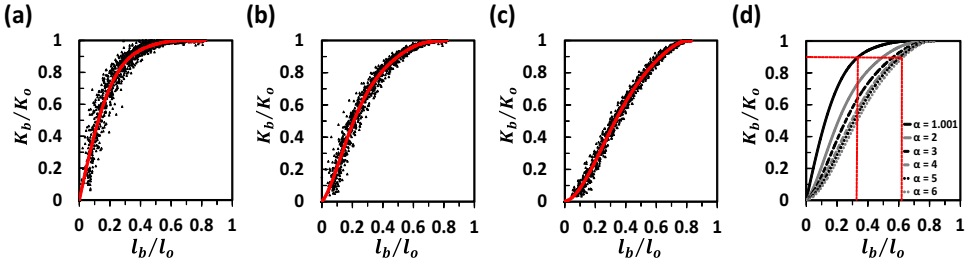

Fig. 3. Equivalent permeability of the dominant sub-network (K_b) normalized by the equivalent permeability of the original fracture network (K_o), plotted against the length of the backbone of the truncated fracture network (l_b) normalized by the total length of the original fracture network (l_o): power-law aperture distributions with (a) $\alpha = 1.001$, (b) $\alpha = 2$ and (c) $\alpha = 6$. Results of 100 realizations shown for each value of α. Red curve is the average trend curve. (d) Average curves from (a–c), including additional values of α. Also shown are values of l_b/l_o retaining 90% of the equivalent network permeability for $\alpha = 1.001$ and $\alpha = 6$, respectively (red dotted lines). (For interpretation of the references to color in this figure legend, the reader is referred to the web version of this article.)

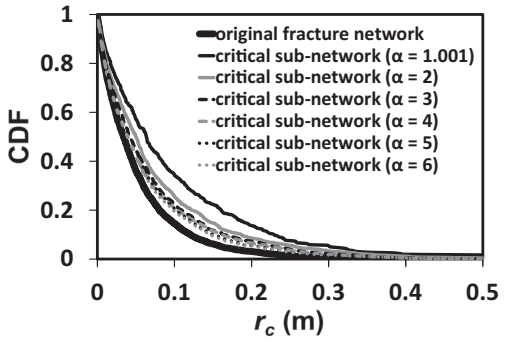

Fig. 4. Cumulative distribution function (CDF) for the characteristic radius of all individual matrix blocks (r_c) formed by the original fracture network (the bottom curve) and the dominant sub-network (retaining 90% of original-network equivalent permeability): power-law aperture distributions with α = 1.001–6. The results of one realization are shown for each value of α.

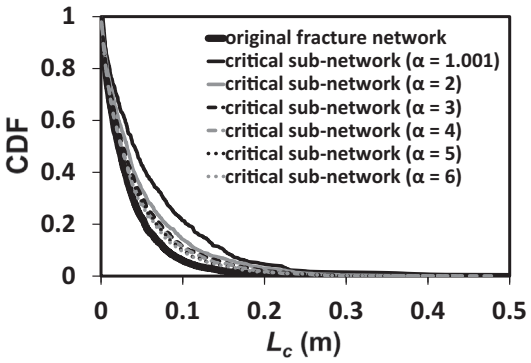

Fig. 6. Cumulative distribution function (CDF) for the characteristic length of all individual matrix blocks (L_c) formed by the original fracture network (the bottom curve) and the dominant sub-network (retaining 90% of original-network equivalent permeability): power-law aperture distributions with α = 1.001–6. The results of one realization are shown for each value of α.

dominant sub-networks for one realization is presented. Similar results are obtained: for the cases with the broadest power-law aperture distribution, the equivalent length for the dominant sub-network is around twice that on average for the original fracture network. The ratio becomes smaller as the aperture distribution is narrower, and decreases to 1.5 for α = 6.

5.2. Results for cases with log-normal aperture distribution

Similar to the results for the cases with power-law aperture distributions, as more fractures are eliminated according to the flow-simulation results, the equivalent matrix-block radius and equivalent matrix-block length become larger for the cases with log-normal aperture distributions (Figs. 7 and 8), and the overall trends are almost unaffected by the breadth of the aperture distribution (Figs. 7d and 8d).

However, the dominant sub-network, defined in our previous study as the sub-network retaining 90% of the original equivalent network permeability after eliminating a portion of fractures, is strongly affected by the aperture distribution: for the broadest aperture distribution cases (σ = 0.6), the flow-path length is roughly 20% of the total length of the original fracture network ($l_b/l_o = 0.2$), while for the narrowest aperture distribution (σ = 0.1), the ratio l_b/l_o is approximately 0.6 (Fig. 9). Correspondingly, as presented in Fig. 7, the ratio between the equivalent radius of the dominant sub-network and that of the entire fracture network (r_e^b/r_e^o) is around 3.5 when σ = 0.6 (the red dashed line in Fig. 7d), which is the broadest aperture distribution examined here. The ratio r_e^b/r_e^o decreases as the aperture distribution becomes narrower, and reaches roughly 1.5 for the cases with the narrowest aperture distribution with σ = 0.1 (the red dotted line in Fig. 7d). The equivalent matrix length (L_e^b) presents similar behaviour as the equivalent matrix radius (Fig. 8).

Similar to our approach with the cases of power-law aperture distributions, we select one realization for each value of σ, and examine the characteristic-radius and characteristic-length distributions of individual matrix blocks in the original fracture network and the dominant sub-network. As presented in Figs. 10 and 11, the characteristic radius and the characteristic length of individual matrix blocks formed by the dominant sub-networks are larger than those of the matrix blocks formed by the entire fracture network.

6. Discussion

Naturally fractured oil reservoirs, like all reservoirs, are exploited in two stages: primary recovery and secondary recovery. The recovery mechanisms are different in these two processes. During primary production, the reservoir is produced by fluid expansion. The pressure drops rapidly in the fractures because of the high permeability, while, in contrast, the matrix remains at higher pressure. This creates a pressure difference between the fracture and the adjacent matrix block, and in turn, leads to flow of oil from the matrix to the fracture. In this scenario, as long as all the fractures are much more conductive than the matrix, one might expect that all connected fractures are conductive enough to bring oil from the matrix to the wells.

In secondary recovery, since the fractures have much higher permeability than the matrix, water from an injection well invades

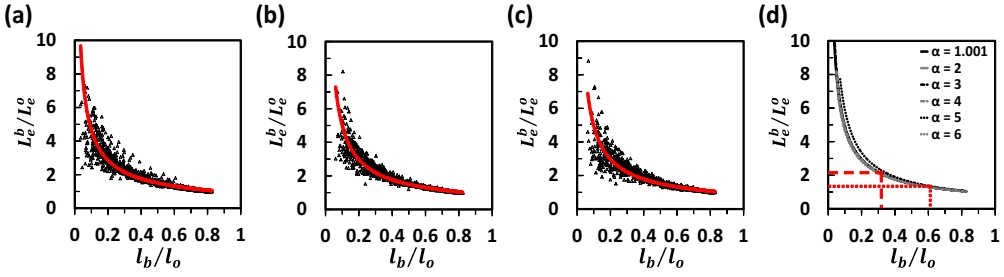

Fig. 5. Equivalent matrix length of the dominant sub-network (L_e^b) normalized by the equivalent matrix length of the original fracture network (L_e^o), plotted against the length of the backbone of the truncated fracture network (l_b) normalized by the total length of the original fracture network (l_o): power-law aperture distributions with (a) α = 1.001, (b) α = 2 and (c) α = 6. Results of 100 realizations are shown for each value of α. The red curve is the average trend curve. (d) average curves from (a–c), including additional values of α. Also shown are values of l_b/l_o for the sub-network retaining 90% of the equivalent network permeability (Fig. 3) and resulting values of L_e^b/L_e^o for α = 1.001 (red dashed line) and α = 6 (red dotted line), respectively. (For interpretation of the references to color in this figure legend, the reader is referred to the web version of this article.)

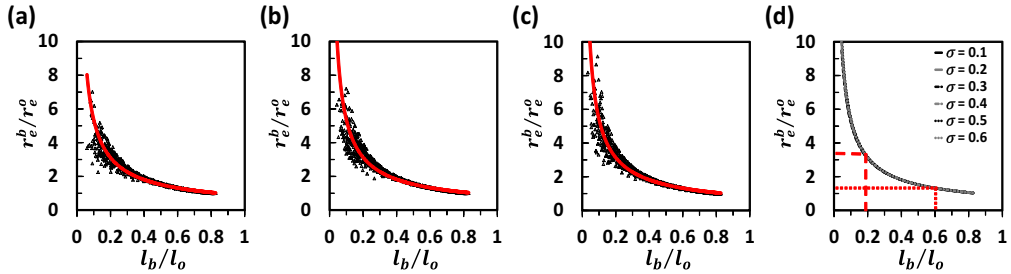

Fig. 7. Equivalent matrix radius of the dominant sub-network (r_e^b) normalized by the equivalent matrix radius of the original fracture network (r_e^o), plotted against the length of the backbone of the truncated fracture network (l_b) normalized by the total length of the original fracture network (l_o): log-normal aperture distributions with (a) $\sigma = 0.1$, (b) $\sigma = 0.2$ and (c) $\sigma = 0.6$. Results of 100 realizations are shown for each value of σ. The red curve is the average trend curve. (d) Average curves from (a–c), including additional values of σ. Also shown are values of l_b/l_o for the sub-network retaining 90% of the equivalent network permeability (Fig. 9) and resulting values of r_e^b/r_e^o for $\sigma = 0.1$ (red dotted line) and $\sigma = 0.6$ (red dashed line), respectively. (For interpretation of the references to color in this figure legend, the reader is referred to the web version of this article.)

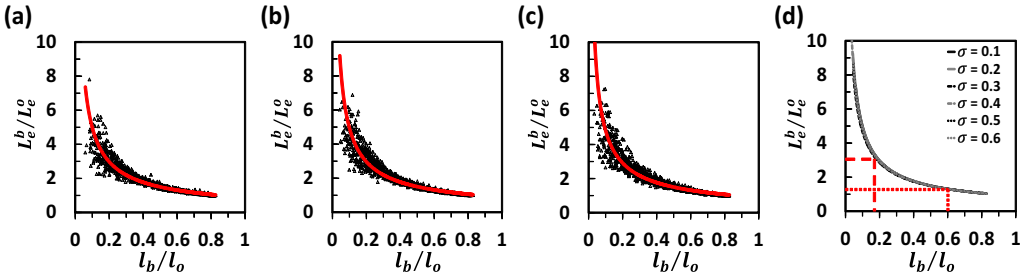

Fig. 8. Equivalent matrix length of the dominant sub-network (L_e^b) normalized by the equivalent matrix length of the original fracture network (L_e^o), plotted against the length of the backbone of the truncated fracture network (l_b) normalized by the total length of the original fracture network (l_o): log-normal aperture distributions with (a) $\sigma = 0.1$, (b) $\sigma = 0.2$ and (c) $\sigma = 0.6$, results of 100 realizations are shown for each value of σ. The red curve is the average trend curve. (d) Average curves from (a–c), including additional values of σ. Also shown are values of l_b/l_o retaining 90% of the equivalent network permeability (Fig. 9) and resulting values of L_e^b/L_e^o for $\sigma = 0.1$ (red dotted line) and $\sigma = 0.6$ (red dashed line), respectively. (For interpretation of the references to color in this figure legend, the reader is referred to the web version of this article.)

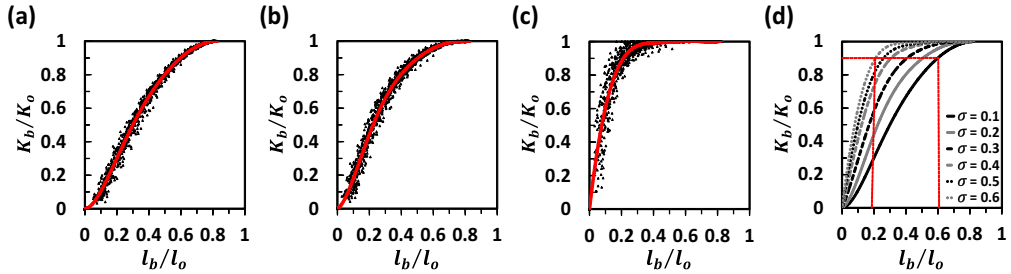

Fig. 9. Equivalent permeability of the dominant sub-network (K_b) normalized by the equivalent permeability of the original fracture network (K_0), plotted against the length of the backbone of the truncated fracture network (l_b) normalized by the total length of the original fracture network (l_o): log-normal aperture distributions with (a) $\sigma = 0.1$, (b) $\sigma = 0.2$ and (c) $\sigma = 0.6$. Results of 100 realizations shown for each value of σ. Red curve is the average trend curve. (d) Average curves from (a–c), including additional values of σ. Also shown are values of l_b/l_o retaining 90% of the equivalent network permeability for $\sigma = 0.1$ and $\sigma = 0.6$, respectively. (For interpretation of the references to color in this figure legend, the reader is referred to the web version of this article.)

the fractures much faster than the matrix. The water rapidly flows through the fracture network and surrounds a matrix block. If the matrix block has water-wet characteristics, water imbibes into the matrix block because of capillary pressure. In many cases, this is a counter-current imbibition process: water and oil flow in opposite directions, although co-current imbibition is faster and can be more efficient than counter-current imbibition [54].

In this case, the cumulative oil recovery from matrix blocks surrounded by water in fractures can be scaled by an exponential equation [55]:

$$R = R_\infty(1 - e^{-\lambda t}) \tag{11}$$

where R is the recovery, R_∞ is the ultimate cumulative recovery, λ is a constant and t is time. Mattax and Kyte [56] redefined the scale equation for imbibition recovery through experimental investigations:

$$R = R_\infty\left(1 - e^{-\lambda_D t_D}\right) \tag{12}$$

where

$$t_D = \left[\sqrt{\frac{k}{\phi}}\left(\frac{\sigma}{\mu_w L_m^2}\right)\right] t \tag{13}$$

and t_D is a dimensionless time, k is the permeability of the matrix block, ϕ is the porosity of the matrix block, σ is the interfacial tension, μ_w is the water viscosity, L_m is the matrix block size, and t is imbibition time.

Kazemi et al. [46] further modified the Mattax and Kyte's scaling equation by introducing the shape factor (F_s), which considered

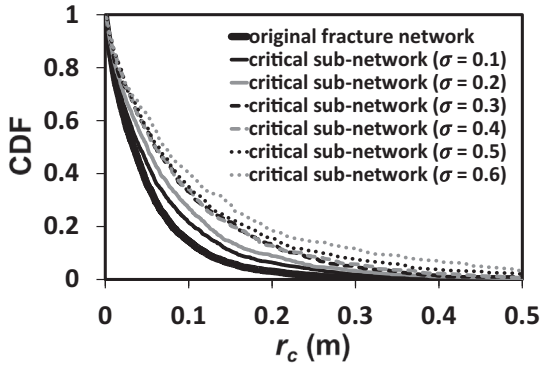

Fig. 10. Cumulative distribution function (CDF) for the characteristic radius of all individual matrix blocks (r_c) formed by the original fracture network (the bottom curve) and the dominant sub-network (retaining 90% of original-network equivalent permeability): log-normal aperture distributions with $\sigma = 0.1$–0.6. The results of one realization are shown for each value of σ.

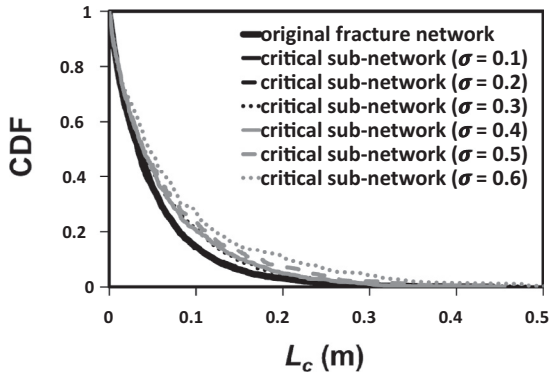

Fig. 11. Cumulative distribution function (CDF) for the characteristic length of all individual matrix blocks (L_c) formed by the original fracture network (the bottom curve) and the dominant sub-network (retaining 90% of original-network equivalent permeability): log-normal aperture distributions with $\sigma = 0.1$–0.6. The results of one realization are shown for each value of σ.

the effect of matrix block shapes and boundary conditions. Eq. (13) becomes

$$t_D = \left[\sqrt{\frac{k}{\phi}}\left(\frac{\sigma F_s}{\mu_w}\right)\right] t \tag{14}$$

$$t_D = \left[\sqrt{\frac{k}{\phi}}\left(\frac{\sigma}{\mu_w L_c^2}\right)\right] t \tag{15}$$

The definitions of the shape factor (F_s) and the characteristic length (L_c) are described in Eqs. (8) and (9). Thus, when the shape factor of a matrix block becomes smaller, or the characteristic length becomes greater, it takes a longer time to recover a certain portion of oil. As presented in Figs. 6 and 11, in general, for all the cases the characteristic length (L_c) of the matrix blocks formed by the dominant sub-networks are larger than that of the matrix blocks formed by the entire fracture networks. This implies that the rate of oil recovery from the matrix blocks is overestimated if the entire fracture network is considered to take part in the water-flooding process.

Eq. (15) is for one matrix block; here we apply this formula to the average value of a series of matrix blocks in order to estimate the effect of matrix block sizes on the speed of oil recovery during the waterflooding process. For the cases with broadest aperture distributions ($\alpha = 1.001$ for a power-law aperture distribution and $\sigma = 0.6$ for a log-normal aperture distribution), the characteristic length (L_c) of the matrix block formed by the dominant sub-networks are on average about twice and three times larger than that formed by the entire fracture networks, respectively (Figs. 5 and 8). This suggests that, for the cases with the broadest power-law aperture distribution, if the entire fracture network is considered to take part in the water-flooding process, the estimated imbibition recovery rate from matrix blocks can be on average four times faster than if only the dominant sub-network is taken into account. For the cases with the broadest log-normal aperture distribution, it can be on average nine times faster. Even for the cases with the narrowest aperture distributions ($\alpha = 6$ for a power-law aperture distribution and $\sigma = 0.1$ for a log-normal aperture distribution), the imbibition recovery process can be more than twice as fast.

As discussed above, most water does not flow through the entire fracture network, but mainly through the dominant sub-network, and the remaining portion of the fractures can be ignored without strongly affecting the overall flow. Considering the recovery mechanism of waterflooding, if the entire fracture network is taken into account, it means we assume the water flows through all the fractures. Then the sizes of matrix blocks formed by fractures and typical fracture spacing are smaller than in the dominant sub-network, which makes the estimated imbibition recovery process faster than it really is. Since dual-porosity/dual-permeability models do not represent fractures explicitly, but assign average properties to grid cells, taking the entire fracture network into account may lead to an inaccurate shape factor, and in turn, give rise to inaccuracy for dual-porosity/dual-permeability simulation of the secondary recovery. The same argument would apply to EOR processes, which depend on penetration of the injected fluid through the fracture network, as waterflooding depends on water.

This suggests that the shape factor for dual-porosity/dual-permeability simulation should depend on the process involved. Specially, it should be different for primary and for secondary or tertiary recovery. For primary recovery, all fractures should be included; for waterflooding or EOR, taking into account only the dominant sub-network which carries almost all water might give a better estimation.

7. Conclusion

Even in a well-connected fracture network, injected water does not flow through the entire fracture network; it mainly flows through a dominant sub-network which is strongly affected by the aperture distribution. The remaining fractures can be ignored without strongly affecting the overall flow through the fracture network.

The typical fracture spacing and sizes of matrix blocks defined by the entire fracture network are generally larger than those formed by the dominant sub-work which carries most of the flow. If the typical fracture spacing used to calculate the shape factor for a waterflooding process accounts for the entire fracture network, it means the water is assumed to flow through all fractures and all fractures participate in the imbibition process, which is not the case. The shape factor calculated by taking all fractures into account may lead to inaccurate dual-porosity/dual-permeability simulation of the water-flood process. A similar argument applies to EOR; the injected EOR agent does not flow equally through all the fractures.

This suggests that the shape factor for dual-porosity/dual-permeability simulation should be different for primary and for secondary recovery and EOR. Specifically, for primary recovery, all fractures should be included, while for the processes in which

delivery of injected fluids plays a limiting role, such as secondary recovery and EOR, the characteristic matrix-block size or shape factor utilised in simulation should be larger.

Acknowledgements

We would like to thank Saudi Aramco and The China Scholarship Council (CSC) for supporting our work.

Reference

[1] Saidi AM. Reservoir engineering of fractured reservoirs (fundamental and practical aspects). Paris: Total Edition Press; 1987.
[2] Moinfar A, Narr W, Hui M-H, Mallison BT, Lee SH. Comparison of discrete-fracture and dual-permeability models for multiphase flow in naturally fractured reservoirs. In: SPE reservoir simulation symposium. The Woodlands, Texas, USA: Society of Petroleum Engineers; 2011.
[3] Barenblatt GI, Zheltov IP, Kochina IN. Basic concepts in the theory of seepage of homogeneous liquids in fissured rocks [strata]. J Appl Math Mech 1960;24:1286–303.
[4] Warren J, Root PJ. The behavior of naturally fractured reservoirs. Soc Petrol Eng J 1963;3:245–55, SPE-426-PA.
[5] Kazemi H, Merrill Jr LS, Porterfield KL, Zeman PR. Numerical simulation of water-oil flow in naturally fractured reservoirs. Soc Petrol Eng J 1976;16:317–26, SPE-5719-PA.
[6] Hill AC, Thomas GW. A new approach for simulating complex fractured reservoirs. In: Middle East oil technical conference and exhibition. Bahrain: Society of Petroleum Engineers; 1985.
[7] Gilman JR, Kazemi H. Improved calculations for viscous and gravity displacement in matrix blocks in dual-porosity simulators (Includes associated papers 17851, 17921, 18017, 18018, 18939, 19038, 19361 and 20174). J Petrol Technol 1988;40:60–70, SPE-16010-PA.
[8] Kim J-G, Deo MD. Finite element, discrete-fracture model for multiphase flow in porous media. AlChE J 2000;46:1120–30.
[9] Karimi-Fard M, Firoozabadi A. Numerical simulation of water injection in fractured media using the discrete-fracture model and the galerkin method. SPE Reservoir Eval Eng 2003;6:117–26, SPE-83633-PA.
[10] Karimi-Fard M, Durlofsky LJ, Aziz K. An efficient discrete-fracture model applicable for general-purpose reservoir simulators. SPE J 2004;9:227–36, SPE-88812-PA.
[11] Geiger S, Roberts S, Matthäi SK, Zoppou C, Burri A. Combining finite element and finite volume methods for efficient multiphase flow simulations in highly heterogeneous and structurally complex geologic media. Geofluids 2004;4:284–99.
[12] Matthäi S, Geiger S, Roberts S, Paluszny A, Belayneh M, Burri A, et al. Numerical simulation of multi-phase fluid flow in structurally complex reservoirs. Geol Soc, London, Special Publ 2007;292:405–29.
[13] Li L, Lee SH. Efficient field-scale simulation of black oil in a naturally fractured reservoir through discrete fracture networks and homogenized media. SPE Reservoir Eval Eng 2008;11:750–8, SPE-103901-PA.
[14] Li L, Lee SH, Jensen C. Method, system and apparatus for simulating fluid flow in a fractured reservoir utilizing a combination of discrete fracture networks and homogenization of small fractures. Google Patents; 2009.
[15] Dershowitz, LaPointe P, Eiben T, Wei L. Integration of discrete feature network methods with conventional simulator approaches. SPE Reservoir Eval Eng 2000;3:165–70, SPE-62498-PA.
[16] Salimi H, Bruining J. Improved prediction of oil recovery from waterflooded fractured reservoirs using homogenization. SPE Reservoir Eval Eng 2010;13:44–55, SPE-115361-PA.
[17] Gong J, Rossen WR. Shape factor for dual-permeability reservoir simulation: effect of non-uniform flow in fracture network. In: ECMOR XIV – 14th European conference on the mathematics of oil recovery EAGE, Catania, Italy.
[18] Dershowitz W, Lee G, Geier J, Foxford T, LaPointe P, Thomas A. User documentation for FracMan. Seattle, Washington: Golder Associates Inc; 2011.
[19] Segall P, Pollard DD. Joint formation in granitic rock of the Sierra Nevada. Geol Soc Am Bull 1983;94:563–75.
[20] Rouleau A, Gale J. Statistical characterization of the fracture system in the Stripa granite, Sweden. Int J Rock Mech Min Sci 1985;22:353–67.
[21] Bour O, Davy P. Connectivity of random fault networks following a power law fault length distribution. Water Resour Res 1997;33:1567–83.
[22] Nicol A, Walsh J, Watterson J, Gillespie P. Fault size distributions—are they really power-law? J Struct Geol 1996;18:191–7.
[23] Odling NE. Scaling and connectivity of joint systems in sandstones from western Norway. J Struct Geol 1997;19:1257–71.
[24] de Dreuzy J-R, Davy P, Bour O. Hydraulic properties of two-dimensional random fracture networks following a power law length distribution: 1. Effective connectivity. Water Resour Res 2001;37:2065–78.
[25] de Dreuzy J-R, Davy P, Bour O. Hydraulic properties of two-dimensional random fracture networks following a power law length distribution: 2. Permeability of networks based on lognormal distribution of apertures. Water Resour Res 2001;37:2079–95.
[26] Barton CC, Hsieh PA, Angelier J, Bergerat F, Bouroz C, Dettinger M, et al. Physical and hydrologic-flow properties of fractures Las Vegas, Nevada—Zion Canyon, Utah—Grand Canyon, Arizona—Yucca Mountain, Nevada July 20–24, 1989. Washington, D.C.: American Geophysical Union; 1989.
[27] Wong TF, Fredrich JT, Gwanmesia GD. Crack aperture statistics and pore space fractal geometry of Westerly granite and Rutland quartzite: implications for an elastic contact model of rock compressibility. J Geophys Res Solid Earth 1989;94:10267–78.
[28] Barton CA, Zoback MD. Self-similar distribution and properties of macroscopic fractures at depth in crystalline rock in the Cajon Pass Scientific Drill Hole. J Geophys Res Solid Earth 1992;97:5181–200.
[29] Belfield W, Sovich J. Fracture statistics from horizontal wellbores. In: SPE/CIM/CANMET international conference on recent advances in horizontal well applications. Petroleum Society Canada; 1994.
[30] Marrett R. Aggregate properties of fracture populations. J. Struct. Geol. 1996;18:169–78.
[31] Ortega O, Marrett R. Prediction of macrofracture properties using microfracture information, Mesaverde Group sandstones, San Juan basin, New Mexico. J Struct Geol 2000;22:571–88.
[32] Snow DT. The frequency and apertures of fractures in rock. Int J Rock Mech Min Sci 1970;7:23–40.
[33] Tsang Y, Tsang C. Channel model of flow through fractured media. Water Resour Res 1987;23:467–79.
[34] Long J, Billaux DM. From field data to fracture network modeling: an example incorporating spatial structure. Water Resour Res 1987;23:1201–16.
[35] Dverstorp B, Andersson J. Application of the discrete fracture network concept with field data: possibilities of model calibration and validation. Water Resour Res 1989;25:540–50.
[36] Cacas M, Ledoux E, de Marsily G, Barbreau A, Calmels P, Gaillard B, et al. Modeling fracture flow with a stochastic discrete fracture network: calibration and validation 2. The transport model. Water Resour Res 1990;26:491–500.
[37] Cacas M, Ledoux E, Marsily Gd, Tillie B, Barbreau A, Durand E, et al. Modeling fracture flow with a stochastic discrete fracture network: calibration and validation: 1. The flow model. Water Resour Res 1990;26:479–89.
[38] Delaney PT, Pollard DD. Deformation of host rocks and flow of magma during growth of minette dikes and breccia-bearing intrusions near Ship Rock, New Mexico. Professional Paper; 1981.
[39] Vermilye JM, Scholz CH. Relation between vein length and aperture. J Struct Geol 1995;17:423–34.
[40] Tsang Y, Tsang C, Hale F, Dverstorp B. Tracer transport in a stochastic continuum model of fractured media. Water Resour Res 1996;32:3077–92.
[41] van Golf-Racht TD. Fundamentals of fractured reservoir engineering. Amsterdam: Elsevier; 1982.
[42] Nick HM, Paluszny A, Blunt MJ, Matthai SK. Role of geomechanically grown fractures on dispersive transport in heterogeneous geological formations. Phys Rev E 2011;84:056301.
[43] Matthäi SK, Belayneh M. Fluid flow partitioning between fractures and a permeable rock matrix. Geophys Res Lett 2004;31:L07602.
[44] Matthai SK, Nick HM. Upscaling two-phase flow in naturally fractured reservoirs. AAPG Bull 2009;93:1621–32.
[45] Cinco-Ley H, Samaniego F, Kucuk F. The pressure transient behavior for naturally fractured reservoirs with multiple block Size. In: SPE annual technical conference and exhibition. Las Vegas, Nevada: Society of Petroleum Engineers; 1985. V.
[46] Kazemi H, Gilman J, Eisharkawy A. Analytical and numerical solution of oil recovery from fractured reservoirs with empirical transfer functions. SPE Reservoir Eng 1992;7:219–27, SPE-19849-PA.
[47] Shouxiang M, Morrow NR, Zhang X. Generalized scaling of spontaneous imbibition data for strongly water-wet systems. J Petrol Sci Eng 1997;18:165–78.
[48] Rodriguez-N R, Cinco-L H, Samaniego-V F. A variable block size model for the characterization of naturally fractured reservoirs. In: SPE annual technical conference and exhibition. New Orleans, Louisiana: Society of Petroleum Engineers; 2001.
[49] Ranjbar E, Hassanzadeh H, Chen Z. One-dimensional matrix-fracture transfer in dual porosity systems with variable block size distribution. Transp Porous Media 2012;95:185–212.
[50] Zimmerman RW, Bodvarsson GS. Effective block size for imbibition or absorption in dual-porosity media. Geophys Res Lett 1995;22:1461–4.
[51] Zhang X, Morrow NR, Ma S. Experimental verification of a modified scaling group for spontaneous imbibition. SPE Reservoir Eng 1996;11:280–5, SPE-30762-PA.
[52] Mirzaei-Paiaman A, Masihi M. Scaling equations for oil/gas recovery from fractured porous media by counter-current spontaneous imbibition: from development to application. Energy Fuels 2013;27:4662–76.
[53] Heinemann Z, Mittermeir G. Derivation of the Kazemi–Gilman–Elsharkawy generalized dual porosity shape factor. Transp Porous Media 2012;91:123–32.
[54] Ramirez B, Kazemi H, Al-kobaisi M, Ozkan E, Atan S. A critical review for proper use of water/oil/gas transfer functions in dual-porosity naturally fractured reservoirs: Part I. SPE Reservoir Eval Eng 2009;12:200–10, SPE-109821-PA.
[55] Aronofsky JS, Masse L, Natanson SG. A model for the mechanism of oil recovery from the porous matrix due to water invasion in fractured reservoirs. Society of Petroleum Engineers; 1958.
[56] Mattax CC, Kyte JR. Imbibition oil recovery from fractured, water-drive reservoir. Soc Petrol Eng J 1962;2:177–84, SPE-187-PA.